Progress in Additive Manufacturing (2025) 10:619–629
https://doi.org/10.1007/s40964-024-00646-5

FULL RESEARCH ARTICLE

Experimental study on the effect of filament-extrusion rate on the structural, mechanical and thermal properties of material extrusion 3D-printed polylactic acid (PLA) products

László Lendvai[1] · Imre Fekete[1] · Daniele Rigotti[2] · Alessandro Pegoretti[2]

Received: 24 January 2024 / Accepted: 26 April 2024 / Published online: 12 May 2024

Abstract
Material extrusion (MEX), also commonly referred to as fused deposition modeling (FDM) or fused filament fabrication (FFF) is currently one of the most commonly used additive manufacturing techniques. The quality of the 3D-printed objects fabricated by MEX methods highly relies on various printing parameters, one of which is the so-called filament extrusion multiplier (k). In this study, 3D-printed parts were prepared by MEX technique during which the material feeding rate was adjusted by varying the extrusion multiplier in the range of 97–105% ($k = 0.97$–1.05). The fabricated parts were tested for their geometrical, structural, mechanical, and thermal conductivity properties. Based on computed tomographic analysis and scanning electron microscopic images, increasing the k parameter resulted in smaller voids, along with gradually decreasing porosity (from 5.82 to 0.05%). Parallel to the decreasing defects, the thermal conductivity of the parts improved from 0.157 to 0.188 W/mK as determined by light-flash analysis technique. On the other hand, when k was set to ≥ 1.03 the geometrical accuracy declined, the size of the specimens considerably increased relative to the nominal values, especially in the X–Y directions due to excess material getting "squeezed" on the sides of the specimens. This latter phenomenon also resulted in the formation of a number of stress concentration sites, which manifested in the decrease of mechanical properties. Accordingly, the tensile, flexural, and impact strength of the samples improved up to $k = 1.03$; however, above that it dropped considerably.

Keywords Material extrusion · Fused filament fabrication · Fused deposition modeling · Process parameters · Extrusion multiplier · Feeding rate · Polylactic acid

1 Introduction

Additive manufacturing (also referred to as 3D printing) technologies have experienced immense development throughout the last three decades [1–4]. In contrast to conventional manufacturing processes, i.e., formative and subtractive methods, additive production is based on the idea of fabricating the desired objects through the addition of material layer by layer. The reason for 3D printing techniques gaining more and more ground is twofold: (i) they allow for the production of complex structures that would be otherwise substantially more complicated or even impossible and (ii) applying these manufacturing methods results in considerably less expenditures and time compared to molding and assembly, especially in the case of individual and short series production [5]. Among others, the demand for additive manufacturing is increasing in aerospace, automotive, and medical industries year by year [6–10]. Currently, there are multiple additive techniques available, all working on the principles of layer-by-layer production. Out of those, material extrusion (MEX)-based 3D printing methods have drawn considerable attention recently [11, 12]. In the literature, MEX additive processes are also generally referred to as fused deposition modelling (FDM) or fused filament fabrication (FFF). The dynamic spread of MEX-based manufacturing devices was greatly facilitated by the so-called *RepRap* project that developed an open-source system for the design and operation of such 3D printers [13, 14].

The MEX 3D printers generally use a thermoplastic material in the form of a filament, which the printer head makes

✉ László Lendvai
lendvai.laszlo@sze.hu

[1] Department of Materials Science and Engineering, Széchenyi István University, H-9026 Gyor, Hungary

[2] Department of Industrial Engineering, University of Trento, 38123 Trento, Italy

molten and then is deposited onto the building platform by being squeezed through a heated nozzle. MEX is compatible with a number of polymers of which the most commonly used ones are acrylonitrile butadiene styrene (ABS) and polylactic acid (PLA) due to their favorable rheological and thermal properties that make them easily processable using this technique [15, 16]. While ABS is a common petrol-based plastic [17], which has been used for decades for this purpose, PLA is an emergent biomaterial. Due to environmental and economic considerations, this latter polymer is used more and more. It is a renewable bio-polyester, which is compostable as well, and due to its lower melting temperature compared to ABS, it also requires less energy to process [18].

Despite the many advantages, MEX-based 3D printing still has certain shortcomings that limit the potential fields of applications, such as the relatively low selection of available materials, which acts as a major driving force both for industrial and scientific research and development to prepare filaments that meet specific requirements regarding their properties while also being workable with extrusion-based 3D printing techniques [15, 19–23]. The other main drawback of MEX additive manufacturing is the lower load capacity of the fabricated parts compared to those that are produced with traditional polymer processing techniques, such as extrusion and injection molding. The mechanical properties of 3D-printed objects are affected by numerous input parameters, including layer thickness, infill strategy, raster angle, infill ratio, temperature of the nozzle and the building platform [24].

The two major factors contributing to the relatively poor mechanical properties of 3D-printed parts compared to the mass-produced ones are the limited interfacial adhesion between the deposited beads and the undesirable, inherent pores/defects that are present in the printed objects. These voids can be classified into five groups according to the mechanism of their formation: (i) raster gap voids, (ii) partial neck growth voids, (iii) sub-perimeter voids, (iv) intra-bead voids, and (v) infill voids [25]. Besides affecting the mechanical behavior, the pores also cause the deterioration of many other properties, including heat conductivity or gas barrier efficiency, which is another reason to strive to eliminate them as much as possible [26–28]. A key factor of these void-type defects is their morphology, which is especially important in the case of the mechanical performance of additively manufactured parts. The shape of voids can be described with a multitude of properties. Most often, void sphericity and compactness are used for this purpose [24].

Among the various settings and parameters that can be adjusted during MEX 3D printing, the extrusion multiplier (k) is the one that determines the volumetric amount of material that is pushed through the printer head/nozzle. Extrusion multiplier can either be defined during the slicing procedure or directly through the control panel of the 3D printer by the user before/during the printing. When k equals 1, then the volume of the extruded material is identical to what the slicer software calculated to be ideal for printing. Slicers are designed to aim for geometrical accuracy, even though that inherently comes with voids and pores within the printed object that deteriorate several other properties. Varying the k parameter can be a logical approach to property-tailor the printed object, however, only a few studies have addressed this topic up to this point [29, 30] and there is still much to investigate to understand the potential it holds. As previous studies have already pointed out [30], when increasing the extrusion rate by a certain percent, the percentile increment of material output would not necessarily be the same, since it is greatly dependent on a number of factors, including the viscosity of the printing material, the diameter of the nozzle, and also on the feeding mechanism. Feeding is mostly performed by a pair of gears that push the filament in the direction of the nozzle. When their rotational speed is increased, the pressure inside the printer head is expected to rise. If the pressure becomes too high, it might result in filament slippage between the gears or, in an extreme scenario, filament crushing might occur as well if the material is brittle.

Based on the available literature, it is clear that by properly adjusting the extrusion rate during MEX-based additive manufacturing, the internal porosity of the 3D-printed objects, and thereby their mechanical properties and thermal conductivity can be fine-tuned/improved at the cost of geometrical accuracy. The ultimate structure–property relationships of 3D-printed parts fabricated with modified k parameters, however, are yet to be discovered. Therefore, in this current study, the effect of extrusion multiplier has been investigated with respect to macrostructure, dimensional accuracy, mechanical properties, and thermal conductivity of the fabricated objects to explore the structure–property relationships. The internal structure and the porosity of the 3D-printed specimens were analyzed by means of computed tomography (CT) and scanning electron microscopy (SEM), the mechanical behavior of the samples was examined through tensile tests, flexural tests, and Charpy-impact tests, while the thermal conductivity values were determined by light-flash method.

2 Experimental

2.1 Specimen fabrication

A Craftbot Plus desktop MEX 3D printer (CraftUnique Ltd., Budapest, Hungary) was used to fabricate the specimens for the various characterization techniques. The filament used as input material to the printer was an “Extrafill Traffic White” grade PLA, obtained from Fillamentum Manufacturing

Czech s.r.o. (Hulín, Czech Republic) that had a nominal diameter of 1.75 mm and a density of 1.24 g/cm^3. The official datasheet reported the diameter tolerance of the filament to be ± 0.05 mm. Due to precaution, the actual size was determined before the experiments using a micrometer caliper and it was found to be in a smaller range of ± 0.02 mm. During the printing process, the nozzle (diameter of 0.4 mm) was heated to 215 °C, while the temperature of the building platform was set to 60 °C. The layer thickness was 0.2 mm, the printing speed was 60 mm/min and the theoretical infill density was 100%. Two contour layers with a thickness of 0.4 mm were applied. The nozzle toolpath was generated using the CraftWare slicer software (1.23 version). Prior to the specimen fabrication, the three axes of the printer were calibrated along with the extruder motor. First, by adjusting the e-steps to have accurate extrusion amounts, then a calibration cube was printed and measured to show that the X, Y, and Z axes are accurate and precise. During the experimental series, the extrusion multiplier (k) was varied directly on the 3D printer in the range of 0.97 to 1.05 in steps of 0.02. All the specimens were printed with a unidirectional infill orientation that was parallel to the length of the specimen (raster angle = 0°). This orientation allows the resulting properties to be comparable to that of bulk PLA products fabricated by other means (e.g., injection molding, compression molding, etc.) using literature data.

2.2 Characterization

2.2.1 Scanning electron microscopy

The SEM micrographs of the fracture surfaces were recorded with a Hitachi S-3400 N scanning electron microscope (Tokyo, Japan) in secondary electron mode using an acceleration voltage of 10 kV. The samples were sputter-coated with gold prior to the SEM analysis. For this purpose, a Quorum SC7620 type sputter-coater (Lewes, UK) was used.

2.2.2 Computed tomographic analysis

Porosity and void morphology were checked using CT. The scanning of the specimens was done using an Yxlon micro-focus X-ray tube system (Hamburg, Germany). The tube voltage and current were set to 190 kV and 0.12 mA. The detector was configured in a 2 × 2 pixel binning mode allowing for a 1024 × 1024 resolution with a detector element pitch of 0.4 mm. The detector was set to 2000 ms integration time and 1620 projections were made during the scan to reduce noise and enhance the quality of the reconstruction. For CT scanning 10 mm long sections were used from the middle of the rectangular specimens. The resulting voxel size was 0.016 mm. The reconstructed volume was analyzed in VGStudioMAX 2.2 software. The specimens were aligned in an identical coordinate system and porosity detection was performed. The overall porosity of the parts was measured as well as the individual properties of the voids. In this work, the morphology of the voids was characterized by revealing the relationships between the projected area of the voids in the X, Y, and Z directions. By projecting the body of the void on a plane the extent of the defect could be measured.

2.2.3 Tensile tests, flexural tests, and Charpy-impact tests

Mechanical properties were examined in the form of tensile tests, flexural tests, and Charpy-impact tests. Tensile tests were conducted on an Instron 5582 testing machine (Norwood, MA, USA) with a 10 kN load cell following the ISO 527 standard. For this purpose, A-type dumbbell-shaped specimens were 3D printed according to the ISO 3167 standard (cross-section: 4 mm × 10 mm, overall length: 170 mm, length of parallel-sided portion: 80 mm). A strictly unidirectional infill was used for the ends of the specimens This type of infill is preferred according to the literature to lessen the probability of failure outside the gauge zone, which is typical for MEX additive manufactured tensile specimens [31]. The tensile tests started at a crosshead speed of 1 mm/min up to 0.3% elongation to determine the Young's modulus and then continued at 5 mm/min. The initial crosshead distance was 100 mm. The tensile tests were repeated five times for all extrusion multipliers to ensure reproducibility.

The flexural properties of the fabricated samples were determined by 3-point bending tests performed on the same Instron 5582 testing machine (Norwood, MA, USA) according to ISO 178. The cross-section of the specimens was 4 mm × 10 mm (width × thickness), the span length was set to 64 mm, and the crosshead speed was 5 mm/min. The flexural tests were repeated five times for all extrusion multipliers to ensure reproducibility.

The impact strength test was performed following the ISO 179 standard on a Ceast 6545 Charpy pendulum (Pianezza, Italy), using a hammer with an impact energy of 2 J and a bearing distance of 62 mm. For this purpose, unnotched specimens with a size of 80 mm × 10 mm × 4 mm were applied. The Charpy-impact tests were repeated five times for all extrusion multipliers to ensure reproducibility. The weight of the Charpy-impact specimens was also measured with a digital weight balance of 0.1 mg accuracy and compared to a reference specimen printed at $k = 1.00$ to see if the modified extrusion multiplier changes the mass in the same trend. Based on the weight measurements it did, the corresponding results are summarized in Table S1 (supplementary materials).

2.2.4 Thermal conductivity measurement

The thermal conductivity measurements were performed using a Netzsch LFA 467 HyperFlash (Selb, Germany) flash thermal conductivity meter at a temperature of 25 °C under an inert N_2 atmosphere. Before the measurement, the samples were coated with colloidal carbon to ensure complete absorption of light by the samples. Shot parameters were voltage of 200 V, pulse width of 600 µs, and area detection diameter of 3.7 mm. The flash method is a widely recognized technique for the determination of thermophysical properties that include thermal diffusivity, specific heat, and consequently thermal conductivity of solid materials [32]. The thermal conductivity measurements were repeated five times for all extrusion multipliers to ensure reproducibility. The geometry of the specimens used for the analyses with a schematic representation of the used infill orientations is shown in Fig. 1.

2.2.5 Statistical analysis

The significance of the data differences was statistically analyzed by one-way variance analysis (ANOVA). Tukey's honest-significance test with a 95% confidence level was used to identify which data groups were significantly different from others.

3 Results and discussion

3.1 Dimensional accuracy

Firstly, the dimensional accuracy of the samples was determined based on the specimens' extensions along the cross-sectional directions (width and height). This measurement was performed using a micrometer caliper (for values below 35 mm) and a vernier caliper (for values of 35 mm and above). Figure 2 depicts the percentile dimensional accuracy

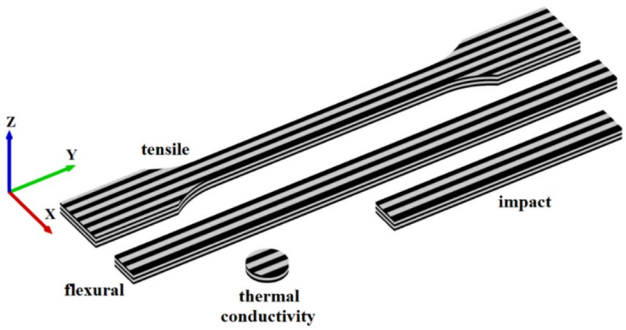

Fig. 1 Schematic graphic of the 3D-printed specimens used for the different analyses (Note: hatching, only represents the orientation of the printed beads, but not their size)

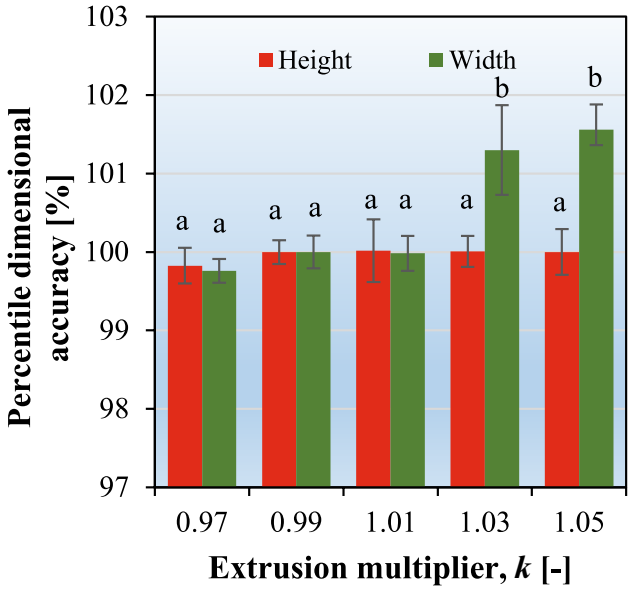

Fig. 2 Percentile dimensional accuracy of the width and height of the printed specimens as a function of extrusion multiplier (identical letters above the bars mean no significant difference according to Tukey's honest-significance test)

of the printed specimens. Considering the height of the specimens (Z direction), it was barely affected by the extrusion multiplier. The lowest *k* parameter of 0.97 resulted in a slightly smaller height of the specimens, above this level, however, there were little to no differences observed compared to the nominal values. The reason for the specimens not exceeding the nominal height even when they are overfilled is that the material is restricted in both directions (+Z and −Z), on the bottom by the build platform and on the top by the printing nozzle's toolpath. On the other hand, the size parameters in the plane of the build platform (length and width) gradually increased at higher *k* values. The effect of under-extrusion is less notable, as it is only influenced by the thinner beads of the shell layer since the printer head always follows the same path according to the G-code. Higher *k* values, however, tend to increase the X–Y extent of the printed objects significantly. Using an extrusion multiplier of 1.03 and 1.05 led to an increment of 1.3% and 1.5%, respectively. It can be attributed to the fact that the excess material was "squeezed" to the sides of the specimens, resulting in uneven, rough-side surfaces, while overflowing in the "Z" direction was not possible as described above.

3.2 Porosity analysis

The voids and pores within the 3D-printed specimens were analyzed both on a micro- and macroscale. For the microscale analysis, SEM images were prepared while the investigation of the macrostructure was carried out through CT

scans. Data from the CT scans was examined with image analysis methods, as well as by visual examination. By observing the cross-sections of the specimens a couple of conclusions can be drawn corresponding to the structure of the voids or defects. In Fig. 3 representative cross-sections can be seen based on CT scans, while Fig. 4 shows the SEM images. Both in Figs. 3 and 4 a continuous decrease in porosity can be identified as the extrusion multiplier is increased. At $k = 0.97$ the increased void size causes some of the neighboring voids to coalesce. From the cross-section images, it can be seen that this behavior is present only in the Z and Y directions, while the beads restrict the merging of voids in the "X" direction. Coalescence in the "Y" direction is reasonable and is inherently present in MEX 3D-printed parts due to the printer head movement direction. The bead deposited along this direction will allow more gap next to the neighboring bead. If the gap is large enough, it forms a contiguous void. A similar merging of voids is also present at k values higher than 0.97, but not as dominantly.

Void coalescence in the Z direction mostly presents itself when the extrusion multiplier is the lowest (Fig. 4a). In this case, the deposited bead's horizontal extent is reduced so much that the previously deposited neighboring beads are barely making contact, if any. The beads are essentially stacked on top of each other in the "Z" direction.

3D visualization of the volumetric porosity in the specimens revealed the previously described mechanism of void coalescence as it is shown in Fig. 5 where the colors of the voids represent their volume in the range of 0 to 1 mm^3. With an increasing extrusion multiplier, the amount of voids gets less and their volume becomes lower. Generally, the higher the k parameter, the lower the volume of the voids, and the less in number. The coalescence of the voids presents itself as defects of very high volume; in Fig. 5 they are colored in purple.

The porosity values of the specimens as a function of k are presented in Fig. 6, based on which a clear relationship can be identified. By increasing the extrusion multiplier, the porosity of the 3D-printed parts can be gradually decreased. The relationship appears to be linear in the range investigated in this current study. It needs to be noted, however, that there necessarily is a limit for this trend where a further increase in the k parameter would not be able to reduce the porosity anymore. In this current case, the porosity is so low (0.05%) at $k = 1.05$ that the printed part can almost be considered as a dense, bulk object. The amount of voids in the specimens is the reason for the previously discussed peculiar mechanism of coalescing voids. By increasing the k factor, the number of detected voids steadily increases until $k = 1.03$, above which a sudden drop can be observed. There seems to be no clear correlation between the porosity and the number of defects. This can be explained by the size of the detected defects being different at different k factors, which is due to the voids coalescing into larger defects when the extruded material amount is not sufficient.

Further investigation of the void morphology involved the projection of individual defects along the three main axes. A schematic visual explanation for the method of projection is

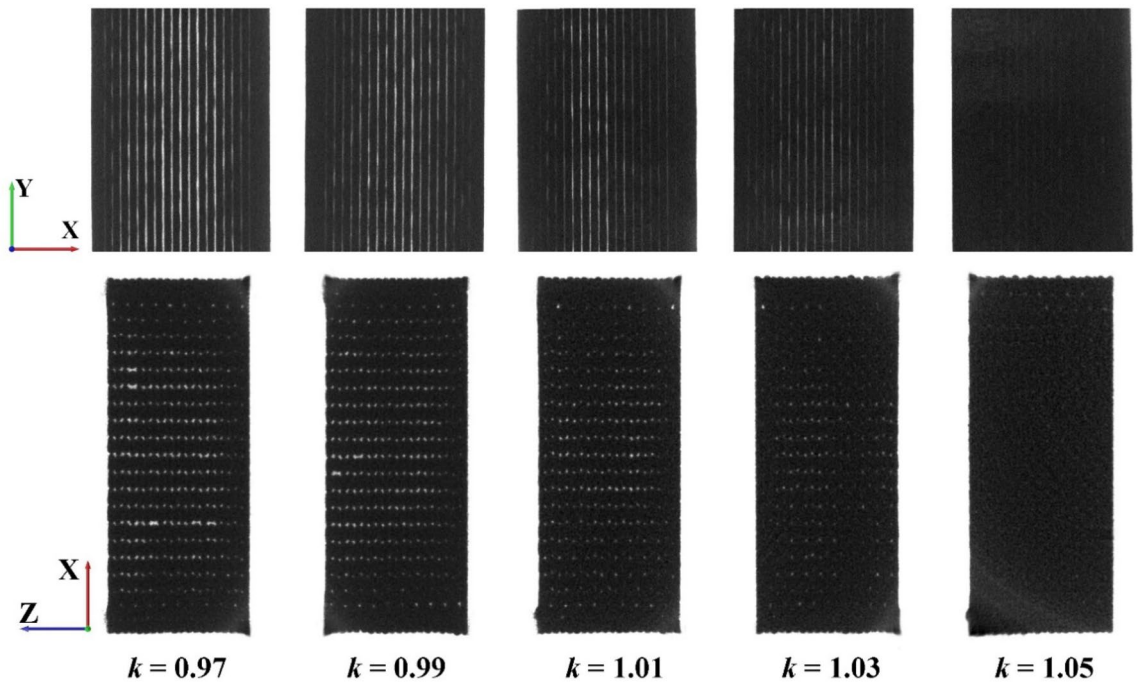

Fig. 3 Top (X–Y) and side view (X–Z) cross-sections of the specimens

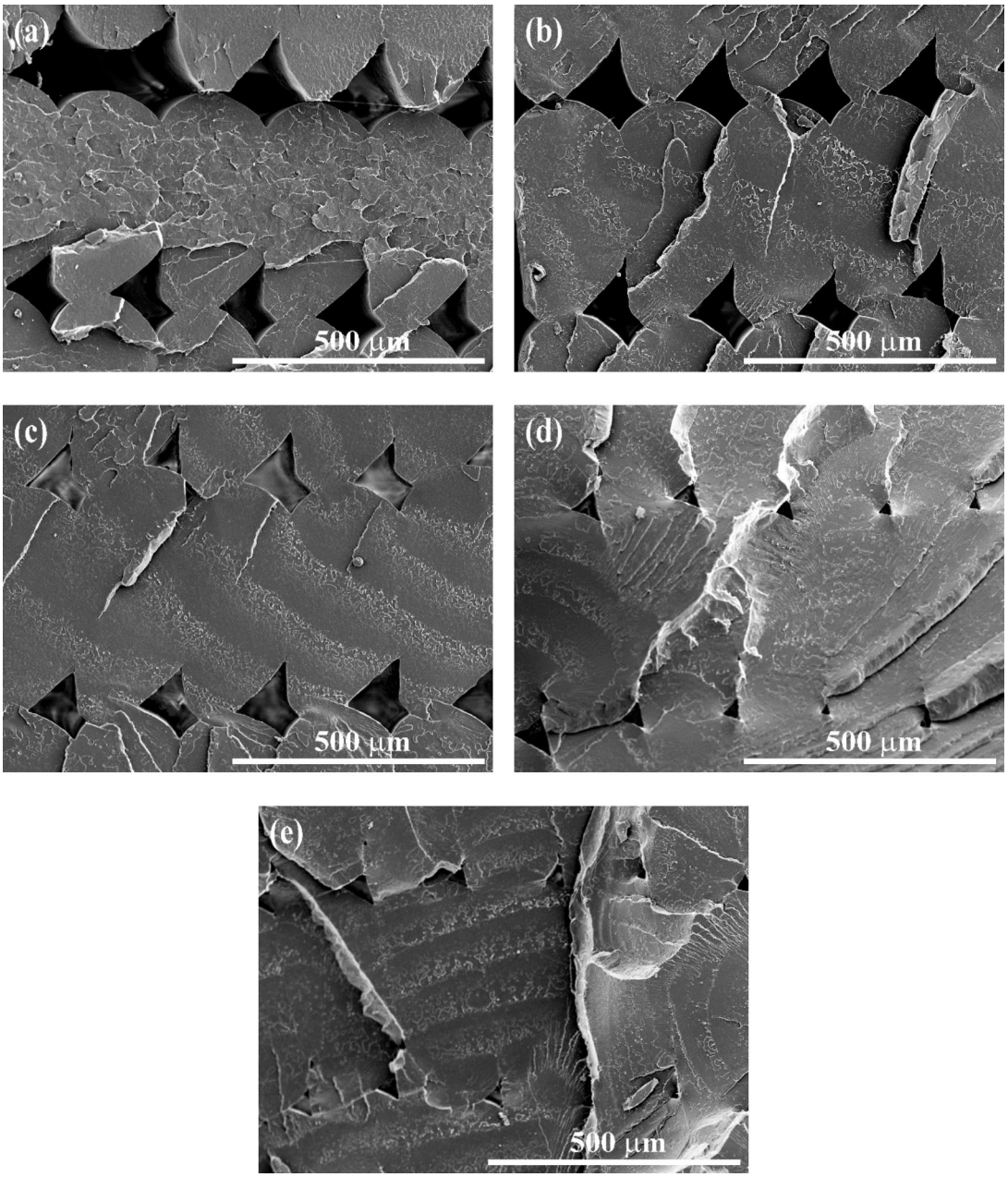

Fig. 4 SEM images of the samples prepared with an extrusion multiplier of $k = 0.97$ (**a**), $k = 0.99$ (**b**), $k = 1.01$ (**c**), $k = 1.03$ (**d**), $k = 1.05$ (**e**)

presented in Fig. S1 (supplementary materials). Each voxel of the void/defect was projected in three directions (X, Y, and Z) and the resulting 2D image was used to calculate the area of the projected surface. The projected areas of the voids were denoted as PX, PY, and PZ depending on which axis the projection was calculated along. PZ is the projected size of the defect along the build direction; PY is the projected area along the length of the printed specimens while PX is the projected area from the side direction or the perpendicular direction to the previous two. Representing the voids this way can provide a better insight into their true extent. As already pointed out in the Introduction, there are various parameters and techniques to describe defects (sphericity, compactness, principal component analysis). However, they can only provide a rough approximation regarding their exact size, which makes the approach used in this current study superior in this regard.

Figure 7 depicts the PZ values of the specimens as a function of PY with the previous parameter shown on a logarithmic scale. The data points are colored so that they represent the value of PX. The straight lines indicate theoretical voids with equal extents in every direction,

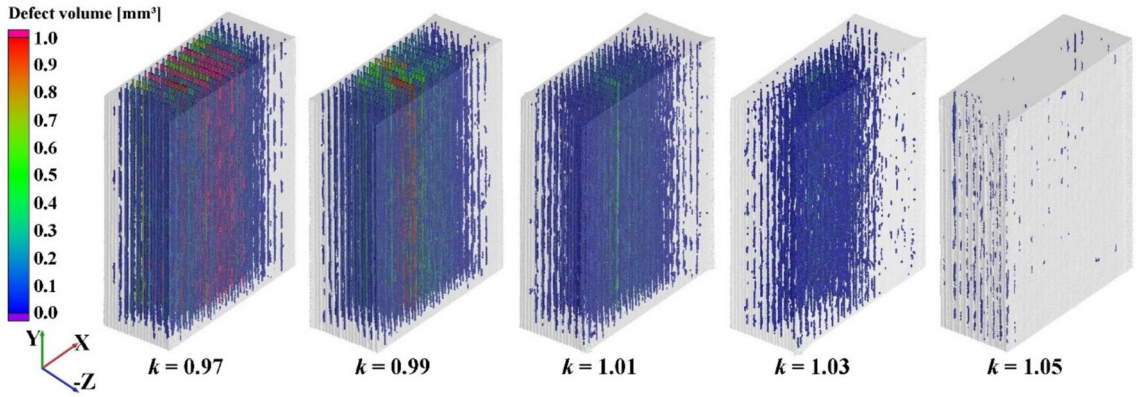

Fig. 5 3D view of the voids in the specimens, colored according to their volume

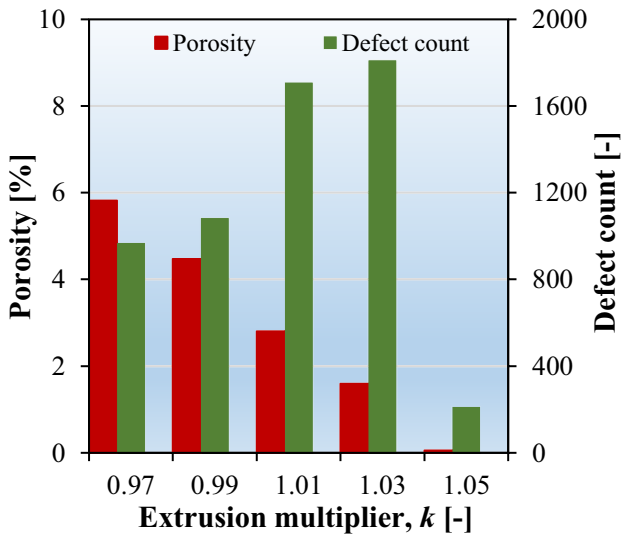

Fig. 6 The number of detected voids and the porosity of specimens at different k factors

where PY = PZ, a scenario which would suggest spherical defect geometries. The PZ size of the voids ranges from 0.00055 to 2.65024 mm^2, while PY ranges from 0.00027 to 0.50591 mm^2, and PX ranges from 0.00055 to 31.06825 mm^2 depending on the extrusion multiplier value. Comparing the data points to the theoretical line of equally sized voids, it is apparent that most of the voids are longer in the Y direction because PY << PZ, suggesting an elongated shape.

With decreasing k factor more and more elongated voids occur due to the coalescence of voids in the "Y" direction. This elongation of the voids is especially prominent at low extrusion multipliers. Note that below $k = 1.01$ coalescence begins in the "Z" direction as well, which is indicated by the drastic increase of PX—the appearance of green, yellow, and red colors in the diagram.

3.3 Tensile and flexural mechanical properties

The tensile and flexural mechanical properties of the specimens prepared with different extrusion multipliers are shown in Fig. 8, while the typical stress–strain curves registered during the tests are shown in Figure S2 (supplementary materials). The lowest tensile strength of 51.1 MPa was measured at $k = 0.97$ and it gradually increased up until $k = 1.03$, where the strength was 57.1 MPa. This latter is close to those values that are measured for PLA materials prepared with processing techniques used in mass production, i.e., injection molding [33–35]. With further growth in the extrusion multiplier, the tensile strength did not improve anymore; on the contrary, a slight reduction to 56.6 MPa was determined for $k = 1.05$, which is somewhat contradicting with the fact that porosity was by far the lowest for this sample (0.05%). The reduction in strength at $k = 1.05$ can be ascribed to the fact that geometry-wise, the over-extrusion led to worse build quality, resulting in more stress concentration sites being formed on the sides of the printed parts due to the excess material being squeezed there. Correlating these results with the porosity data it can be assumed that the number of defects in the specimens has a marginal influence on the strength, while the size of the voids and the surface quality affects the mechanical behavior markedly. Interestingly, in a previous study [30] the authors reported a gradually increasing strength as a function of extrusion multiplier, even at $k = 1.2$. In their study, however, the specimens were machined out of larger 3D-printed blocks, which means that their specimens had a smooth side surface, and as such, the surface quality did not interfere with the mechanical behavior. In this respect, the current study represents the mechanical features of 3D-printed objects more accurately. Regarding the modulus values, the sample printed with the lowest extrusion multiplier exhibited the lowest value of 2920 MPa, and it gradually grew with the increasing of k, the highest (3102 MPa) was at $k = 1.05$, even though there

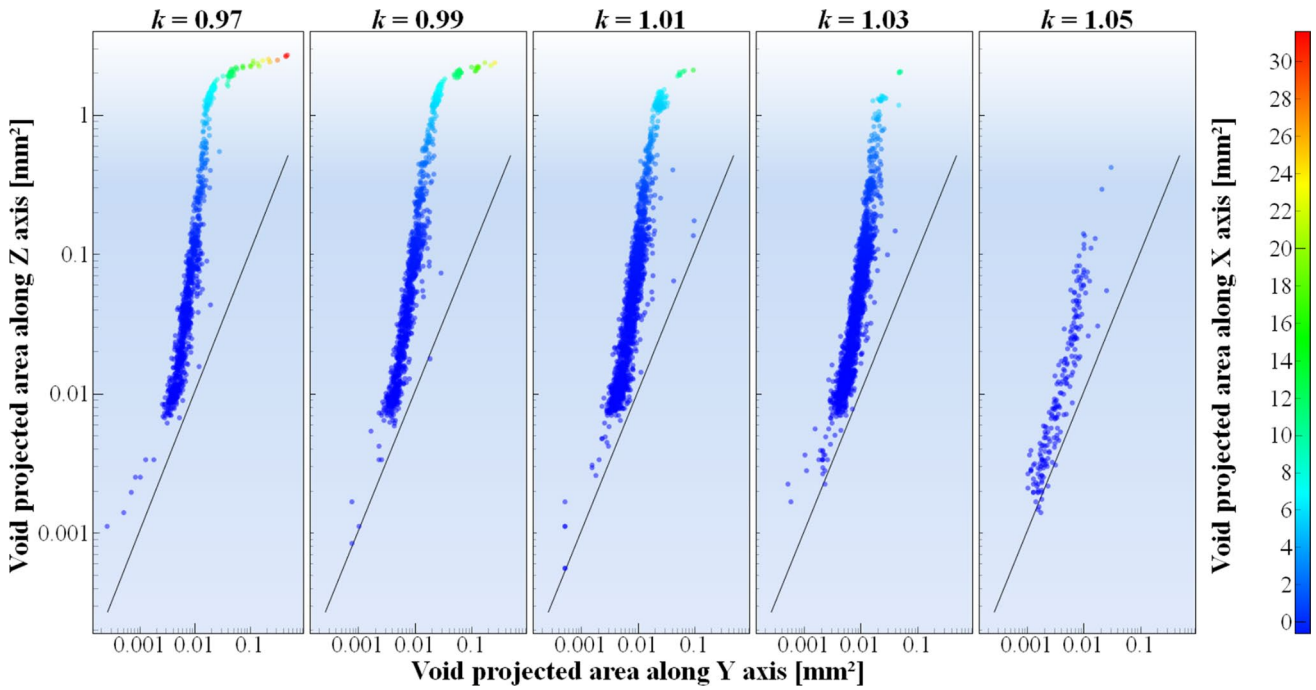

Fig. 7 Projected void sizes detected in the specimens at different *k* factors

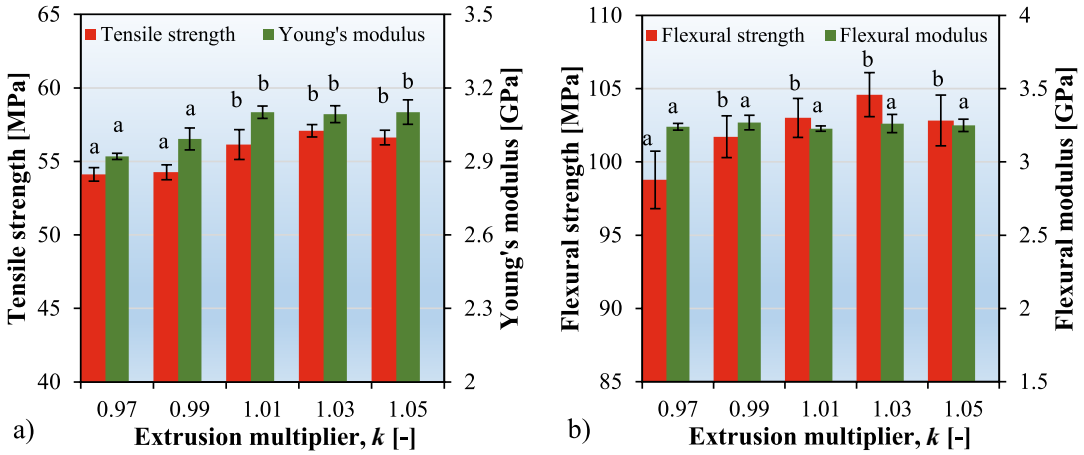

Fig. 8 Variation of (**a**) tensile strength; tensile modulus, and (**b**) flexural strength; flexural modulus as a function of extrusion multiplier (identical letters above the bars mean no significant difference according to Tukey's honest-significance test)

was barely any change between 1.01 and 1.05. The reason for Young's modulus values not decreasing at high extrusion multipliers is the fact that the uneven features of the surface acting as stress concentration sites do not play a crucial role at low levels of mechanical loads, at which stage Young's modulus is calculated. Ultimately, based on the tensile-test results the optimal *k* parameter is 1.03; however, according to the statistical analysis, there is no significant difference in either the strength or the stiffness between $k = 1.01$ and 1.05.

Similar to the tensile strength, the flexural strength (Fig. 8b) was also lowest when the extrusion multiplier was set to 0.97 (98.8 MPa), then it gradually improved, peaking at $k = 1.03$ (104.6 MPa) above which it marginally deteriorated, which further supports the claims made at the tensile tests. Meanwhile, the flexural modulus values only improved slightly as a function of *k*, with all specimens being within the deviation range (3225–3270 MPa). The variance analysis also pointed out that the modulus values were not significantly different in this case. Photographic images of the broken tensile and flexural specimens after testing are shown in Figure S3.

Note that both the determined strength and modulus parameters discussed above are apparent values, meaning they do not represent the properties of the polymeric material but that of the printed object. The explanation for this is that during the mechanical stress calculations, the cross-section was considered to be "bulk" without any pores or voids, which—as seen previously—does not reflect reality. The foremost reason for choosing this approach is that application-wise the users involved in 3D printing are more interested in the load-bearing capacity of the printed object, rather than the material.

3.4 Impact strength

Figure 9 shows the experimental data of Charpy–impact tests. The findings showed that there is a growing trend in energy absorption of impacts as the multiplier of extrusion increases in the range of 0.97–1.03, but a drop can be observed above $k = 1.03$. These results indicate that the presence of porosity is undesirable considering the impact strength of the 3D-printed objects. Similar results have already been reported in studies, where the infill density—which also markedly affects porosity—was varied during the 3D-printing process. Statistically, there is no difference between the multipliers of 0.97, 0.99, and 1.01 concerning the Charpy-impact strength. The drop experienced above $k = 1.03$ from 19.1 to 16.9 kJ/m^2 can again be ascribed to the rougher surface of the samples fabricated at the highest extrusion multiplier. The relative drop in this parameter is 9%, which is considerably larger than those experienced in tensile strength (1%) and flexural strength (2%) values. The reason for this is that polymeric materials are much more sensitive to stress concentration sites when exposed to high-velocity, impact-like mechanical loads. Note, that the Charpy-impact strength of specimens printed at $k = 1.03$ are similar to that of PLA materials prepared with processing techniques used in mass production, i.e., injection molding [34]. Photographic images of the broken impact test specimens after testing are shown in Figure S3 (supplementary materials).

3.5 Thermal conductivity

When an object is fabricated through MEX-based 3D printing, the thermal conductivity of the built part is expected to differ from the thermal conductivity of the bulk polymer due to the inherent presence of voids and gaps [36]. As pointed out in Sect. 3.2. (Porosity analysis), adjusting the extrusion multiplier during MEX-based 3D printing greatly affects the size and amount of the resulting voids. According to the literature, the thermal conductivity of PLA is in the range of 1.57 to 1.85 W/mK [37, 38], while that of air is much lower, 0.024 W/mK. Consequently, with the elimination of voids through increasing the extrusion multiplier, the thermal transport properties of the printed parts may also be improved. The influence of the k parameter on the thermal conductivity is presented in Fig. 10. In general, it can be concluded that the thermal conductivity values of all

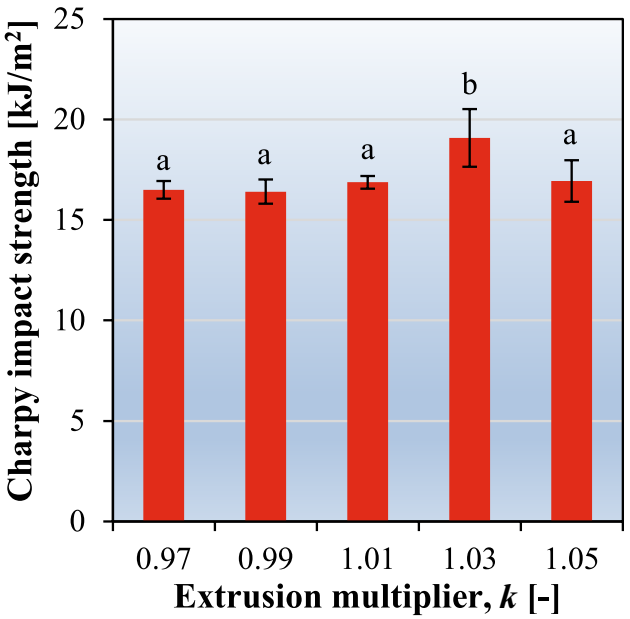

Fig. 9 Variation of Charpy-impact strength as a function of extrusion multiplier (identical letters above the bars mean no significant difference according to Tukey's honest-significance test)

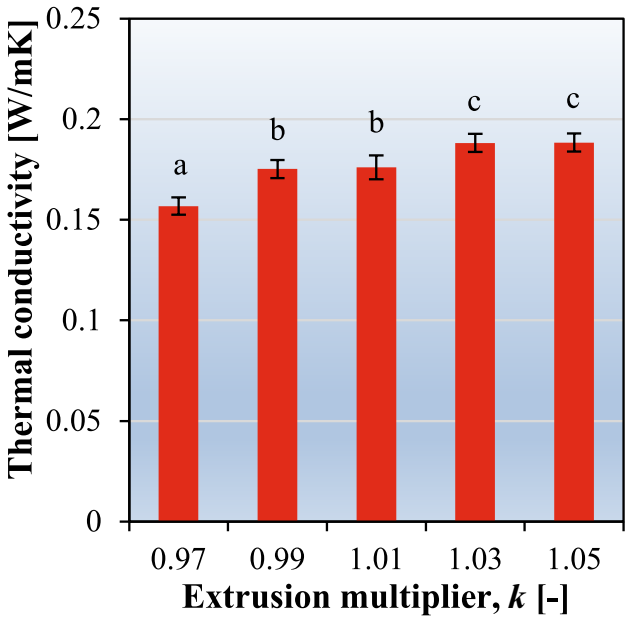

Fig. 10 Variation of thermal conductivity as a function of extrusion multiplier (identical letters above the bars mean no significant difference according to Tukey's honest-significance test)

samples are close to those values reported for PLA in the literature. As expected, the lowest conductivity (0.157 W/mK) was measured for the specimen 3D printed at $k = 0.97$. With increasing extrusion multiplier, the thermal conductivity gradually improved to 0.172, 0.176, 0.188, and 0.188 W/mK when using a k parameter of 0.99, 1.01, 1.03, and 1.05, respectively. Based on these results, from the thermal conductivity point of view it seems reasonable to increase the extrusion multiplier up to 1.03 during the 3D printing process. Above that, however, it is not justified, since the porosity is in such a low range ($< 1.5\%$) where it barely affects this parameter anymore.

4 Conclusion

This study investigated the effect of extrusion multiplier (k) during a MEX-based 3D-printing process. The effect of the k parameter was analyzed in the range of 0.97 to 1.05 for the geometrical, structural, mechanical, and thermal conductivity properties of the 3D-printed PLA parts. Commercial slicing softwares are optimized for the geometrical accuracy of the fabricated objects, which is inherently adjoined with less-than-ideal mechanical properties and thermal conductivity due to the presence of defects in the form of voids. Through experimental investigation, it was shown that increasing the extrusion multiplier up to 1.03 is an effective way to improve the mechanical and, thermal properties of 3D-printed objects at the cost of a slight decrease in the dimensional accuracy along the X and Y axes. According to the performed tests, there was a relative difference of 6% in tensile strength, 6% in Young's modulus, 16% in impact strength, and 20% in thermal conductivity between the specimens printed at $k = 0.97$ and $k = 1.03$ with the latter being superior in all listed properties. Below a k factor of 1.03, the deterioration of properties was ascribed to an increase in void sizes inside the specimens. At low extrusion multipliers immense coalescing of the pores occurred, which drastically increased their size, and thereby facilitated the drop in the examined properties. These claims were also supported through CT scans and SEM images. On the other hand, at $k = 1.05$, the over-extrusion led to a decline in the side surface quality of the samples, which also resulted in reduced mechanical properties, even though the porosity still decreased, indicating that an extrusion multiplier of 1.03 was optimal concerning the investigated properties.

Supplementary Information The online version contains supplementary material available at https://doi.org/10.1007/s40964-024-00646-5.

Author contributions Each author participated sufficiently in the work. L.L. and I.F. produced the samples. L.L., I.F and D.R. performed the analyses. L.L., I.F., D.R. and A.P. wrote the main manuscript text. All authors reviewed the manuscript.

Funding Open access funding provided by Széchenyi István University (SZE). L. Lendvai is grateful for the support of the János Bolyai Research Scholarship of the Hungarian Academy of Sciences. The research presented in this paper was also funded by the "Thematic Excellence Programme 2021 (TKP2021) – National Defence, National Security Subprogramme at the Széchenyi István University (TKP2021-NVA-23).

Declarations

Conflict of interest The authors have no competing interests as defined by Springer, or other interests that might be perceived to influence the results and/or discussion reported in this paper.

References

1. Ngo TD, Kashani A, Imbalzano G, Nguyen KTQ, Hui D (2018) Additive manufacturing (3D printing): a review of materials, methods, applications and challenges. Compos B Eng 143:172–196
2. Gao W, Zhang Y, Ramanujan D, Ramani K, Chen Y, Williams CB, Wang CCL, Shin YC, Zhang S, Zavattieri PD (2015) The status, challenges, and future of additive manufacturing in engineering. Comput Aided Des 69:65–89
3. Kocsis B, Fekete I, Varga LK (2020) Metallographic and magnetic analysis of direct laser sintered soft magnetic composites. J Magn Magn Mater 501:166425
4. Hatos I, Fekete I, Ibriksz T, Kovács JG, Maros MB, Hargitai H (2018) Surface modification and wear properties of direct metal laser sintered hybrid tools used in moulds. J Mech Eng 64:121–129
5. Medel F, Abad J, Esteban V (2022) Stiffness and damping behavior of 3D printed specimens. Polym Testing 109:107529
6. Altıparmak SC, Xiao B (2021) A market assessment of additive manufacturing potential for the aerospace industry. J Manuf Process 68:728–738
7. Salmi M (2021) Additive manufacturing processes in medical applications. Materials 14:191
8. Yadav DK, Srivastava R, Dev S (2020) Design and fabrication of ABS part by FDM for automobile application. Mater Today Proc 26:2089–2093
9. Placone JK, Engler AJ (2018) Recent advances in extrusion-based 3D printing for biomedical applications. Adv Healthc Mater 7:1701161
10. Mohd Pu'ad NAS, Abdul Haq RH, Mohd Noh H, Abdullah HZ, Idris MI, Lee TC (2020) Review on the fabrication of fused deposition modelling (FDM) composite filament for biomedical applications. Mater Today Proc 29:228–232

11. Patiño-Almanza R, Flores-Hernandez CG, Rivera-Armenta JL, Strachota A, Almendarez-Camarillo A (2022) 3D printing of a composite iPP/quill of chicken feathers functionalized with pimelic acid. Polym Compos 43:8914–8924
12. Devarajan B, Lakshmi Narasimhan R, Venkateswaran B, Mavinkere Rangappa S, Siengchin S (2022) Additive manufacturing of jute fiber reinforced polymer composites: a concise review of material forms and methods. Polym Compos 43:6735–6748
13. Pearce JM, Blair CM, Laciak KJ, Andrews R, Nosrat AH, Zelenika-Zovko I (2010) 3-D printing of open source appropriate technologies for self-directed sustainable development. J Sustain Dev 3:17
14. Tymrak BM, Kreiger M, Pearce JM (2014) Mechanical properties of components fabricated with open-source 3-D printers under realistic environmental conditions. Mater Des 58:242–246
15. Andrzejewski J, Cheng J, Anstey A, Mohanty AK, Misra M (2020) Development of toughened blends of poly(lactic acid) and poly(butylene adipate-co-terephthalate) for 3D printing applications: compatibilization methods and material performance evaluation. Acs Sustain Chem Eng 8:6576–6589
16. Khan I, Neeraj K, Yadav JS, Choudhary M, Chauhan A, Singh T (2023) Utilization of waste slate powder in poly(lactic acid) based composite for 3D printer filament. J Mater Res Technol 24:703–714
17. Lendvai L, Rigotti D (2023) Thermal and thermomechanical properties of boron nitride-filled acrylonitrile butadiene styrene (ABS) composites. Acta Technica Jaurinensis 16:123–128
18. Wittbrodt B, Pearce JM (2015) The effects of PLA color on material properties of 3-D printed components. Addit Manuf 8:110–116
19. Coppola B, Cappetti N, Di Maio L, Scarfato P, Incarnato L (1947) 3D Printing of PLA/clay nanocomposites: influence of printing temperature on printed samples properties. Materials 2018:11
20. Kariz M, Sernek M, Obućina M, Kuzman MK (2018) Effect of wood content in FDM filament on properties of 3D printed parts. Mater Today Commun 14:135–140
21. Zhang Q, Cai H, Zhang A, Lin X, Yi W, Zhang J (2018) Effects of lubricant and toughening agent on the fluidity and toughness of poplar powder-reinforced polylactic acid 3D printing materials. Polymers 10:932
22. Lendvai L, Fekete I (2020) Preparation and characterization of poly(lactic acid)/boehmite alumina composites for additive manufacturing. IOP Conf Ser Mater Sci Eng 903:012057
23. Tóth C, Kovács NK (2020) Characterization of short fiber-reinforced polylactic acid composites produced with fused filament fabrication (FFF). IOP Conf Ser Mater Sci Eng 903:012031
24. Vidakis N, David C, Petousis M, Sagris D, Mountakis N, Moutsopoulou A (2022) The effect of six key process control parameters on the surface roughness, dimensional accuracy, and porosity in material extrusion 3D printing of polylactic acid: prediction models and optimization supported by robust design analysis. Adv Ind Manuf Eng 5:100104
25. Tao Y, Kong F, Li Z, Zhang J, Zhao X, Yin Q, Xing D, Li P (2021) A review on voids of 3D printed parts by fused filament fabrication. J Market Res 15:4860–4879
26. Guo H, Zhao H, Niu H, Ren Y, Fang H, Fang X, Lv R, Maqbool M, Bai S (2021) Highly thermally conductive 3D printed graphene filled polymer composites for scalable thermal management applications. ACS Nano 15:6917–6928
27. Cai Z, Thirunavukkarasu N, Diao X, Wang H, Wu L, Zhang C, Wang J (2022) Progress of polymer-based thermally conductive materials by fused filament fabrication: a comprehensive review. Polymers (Basel) 14:4297
28. Gordeev EG, Galushko AS, Ananikov VP (2018) Improvement of quality of 3D printed objects by elimination of microscopic structural defects in fused deposition modeling. PLoS ONE 13:e0198370
29. Bail R (2018) Extrusion temperature and flow rate effects on tensile properties of additively processed poly(ethylene-co-trimethylene terephthalate). Defect Diffus Forum 382:104–108
30. Ghorbani J, Koirala P, Shen Y-L, Tehrani M (2022) Eliminating voids and reducing mechanical anisotropy in fused filament fabrication parts by adjusting the filament extrusion rate. J Manuf Process 80:651–658
31. Fisher T, Almeida JHS Jr, Falzon BG, Kazancı Z (2023) Tension and compression properties of 3D-printed composites: print orientation and strain rate effects. Polymers 15:1708
32. Min S, Blumm J, Lindemann A (2007) A new laser flash system for measurement of the thermophysical properties. Thermochim Acta 455:46–49
33. Tábi T, Ageyeva T, Kovács JG (2022) The influence of nucleating agents, plasticizers, and molding conditions on the properties of injection molded PLA products. Materi Today Commun 32:103936
34. Lendvai L (2023) Lignocellulosic agro-residue/polylactic acid (PLA) biocomposites: Rapeseed straw as a sustainable filler. Clean Mater 9:100196
35. Juhász Z, Pinke B, Gonda B, Mészáros L (2024) Effects of carbon-based nanoparticles on the properties of poly(lactic acid) hybrid composites containing basalt fibers and carbon-based nanoparticles processed by injection molding. Polym Eng Sci. https://doi.org/10.1002/pen.26704
36. Prajapati H, Ravoori D, Woods RL, Jain A (2018) Measurement of anisotropic thermal conductivity and inter-layer thermal contact resistance in polymer fused deposition modeling (FDM). Addit Manuf 21:84–90
37. Spinelli G, Kotsilkova R, Ivanov E, Georgiev V, Naddeo C, Romano V (2022) Thermal and dielectric properties of 3D printed parts based on polylactic acid filled with carbon nanostructures. Macromol Symp 405:2100244
38. Blanco I, Cicala G, Recca G, Tosto C (2022) Specific heat capacity and thermal conductivity measurements of PLA-based 3D-printed parts with milled carbon fiber reinforcement. Entropy 24:654